IOPscience iopscience.iop.org

Home Search Collections Journals About Contact us My IOPscience

Time dependent evolution of RF-generated non-thermal particle distributions in fusion plasmas

This content has been downloaded from IOPscience. Please scroll down to see the full text.

2014 Plasma Phys. Control. Fusion 56 045007

(http://iopscience.iop.org/0741-3335/56/4/045007)

View the table of contents for this issue, or go to the journal homepage for more

Download details:
This content was downloaded by: jungpyo
IP Address: 216.165.95.69
This content was downloaded on 26/09/2014 at 16:04

Please note that terms and conditions apply.

IOP Publishing Plasma Physics and Controlled Fusion

Plasma Phys. Control. Fusion **56** (2014) 045007 (9pp) doi:10.1088/0741-3335/56/4/045007

Time dependent evolution of RF-generated non-thermal particle distributions in fusion plasmas

J C Wright[1], A Bader[1], L A Berry[2], P T Bonoli[1], R W Harvey[3], E F Jaeger[4], J-P Lee[1], A Schmidt[6,7], E D'Azevedo[2], I Faust[1], C K Phillips[5] and E Valeo[5]

[1] Plasma Science and Fusion Center, Massachusetts Institute of Technology, Cambridge, MA 02139, USA
[2] Oak Ridge National Laboratory, Oak Ridge, TN 37831, USA
[3] CompX, Del Mar, CA 92014, USA
[4] XCEL Engineering, Oak Ridge, TN 37830, USA
[5] Princeton Plasma Physics Laboratory, Princeton, NJ 08543, USA
[6] Lawrence Livermore National Laboratory, Livermore, CA 94550, USA

E-mail: jcwright@mit.edu

Received 24 October 2013, revised 22 January 2014
Accepted for publication 20 February 2014
Published 27 March 2014

Abstract

We describe fully self-consistent time-dependent simulations of radio frequency (RF) generated ion distributions in the ion cyclotron range of frequencies and RF-generated electron distributions in the lower hybrid range of frequencies using combined Fokker–Planck and full wave electromagnetic field solvers. In each regime, the non-thermal particle distributions have been used in synthetic diagnostic codes to compare with diagnostic measurements from experiment, thus providing validation of the simulation capability. The computational intensive simulations require multiple full wave code runs that iterate with a Fokker–Planck code. We will discuss advanced algorithms that have been implemented to accelerate both the massively parallel full wave simulations as well as the iteration with the distribution code. A vector extrapolation method (Sidi A 2008 *Comput. Math. Appl.* **56**) that permits Jacobian-free acceleration of the traditional fixed point iteration technique is used to reduce the number of iterations needed between the distribution and wave codes to converge to self-consistency. The computational burden of the parallel full wave codes has been reduced by using a more efficient two level parallel decomposition that improves the strong scaling of the codes and reduces the communication overhead.

Keywords: RF, lower hybrid, ICRF, Fokker–Planck, simulation

(Some figures may appear in colour only in the online journal)

1. Introduction

Radio frequency (RF) power in plasmas injected from antennas and waveguides can create flows, modify the magnetic topology with driven currents and help raise the temperature to trigger fusion reactions through heating of ions and electrons [1]. The amplitudes of externally driven RF waves for use in fusion relevant plasmas induce harmonic perturbations in the plasma that are small compared to the background density and fields. In addition, the wave periods are much shorter than the time scales on which the target plasma evolves. The physics of these waves are described by Maxwell's equations in a dielectric media with the qualification that, because charges are free to move in the plasma, there is no distinction between conduction and polarization currents. The plasma dielectric tensor is formally a non-local integral operator derived from the Vlasov equation for the plasma particle distribution as perturbed by the RF fields [2, p 250].

[7] Formerly at PSFC, MIT.

 © 2014 IOP Publishing Ltd Printed in the UK

Results from two wave codes are discussed in this article. The All Orders Spectral Algorithm (AORSA) [3] and the TORoidal Lower Hybrid code (TORLH) [4, 5], are applied to the solution of the wave equation (WE) as shown in equation (1) for the ion cyclotron range of frequencies (ICRFs) and lower hybrid range of frequencies (LHRFs) respectively. Formulated in the frequency domain, the plasma RF WE is an elliptic system for the rapidly oscillating wave electric field $\boldsymbol{E}$. We note that the system is only formally elliptic in a uniform plasma—in an inhomogeneous plasma, the dielectric introduces higher order operators that make a formal classification as elliptic problematic. The plasma response is represented by $\boldsymbol{J}^{\mathrm{P}}$, which is, in general, given by an integral operator proportional to the wave electric field, $\overleftrightarrow{\sigma}_{\mathrm{c}}$. The wave frequency is ω and $\boldsymbol{J}^{\mathrm{A}}$ is the antenna current driving the RF response. The decomposition used in TORLH is given by equation (1*b*) which uses a toroidal coordinate system with a spectral basis in the periodic dimensions θ and ϕ and a finite element basis for the flux or radial dimension, r to produce a Galerkin weak variational formulation of the differential system. In TORLH a finite electron Larmor radius (FLR) expansion of the dielectric appropriate is used for the LHRF and contributes additional radial derivatives. The AORSA code decomposes the fields in spectral basis in all three coordinates of the cylindrical system (R, Z, ϕ) as shown in equation (1*c*) and retains the full integral dielectric response. The resulting collocation formulation is truncated at a cyclotron harmonic appropriate for the frequency domain of a given problem. Numerically, TORLH produces a block tri-diagonal matrix for inversion and AORSA produces a fully dense matrix.

$$\boldsymbol{\nabla}\times\boldsymbol{\nabla}\times\boldsymbol{E}=\frac{\omega^2}{c^2}\left\{\boldsymbol{E}+\frac{4\pi\mathrm{i}}{\omega}\left(\boldsymbol{J}^{\mathrm{P}}+\boldsymbol{J}^{\mathrm{A}}\right)\right\} \tag{1a}$$

$$\boldsymbol{E}(r,\theta,\phi)=\sum_m \boldsymbol{E}_m(r)\exp\left(\mathrm{i}m\theta+\mathrm{i}n\phi\right) \tag{1b}$$

$$\boldsymbol{E}(R,Z,\phi)=\sum_{n,m,l}\boldsymbol{E}_{n,m,l}\exp\left(\mathrm{i}(k_nR+k_mZ+l\phi)\right) \tag{1c}$$

$$\boldsymbol{J}^{\mathrm{P}}(\boldsymbol{x})=\sum_i\overleftrightarrow{\sigma}_{\mathrm{c}}\left(\boldsymbol{k}^{(i)},\boldsymbol{x}\right)\cdot\boldsymbol{E}_i(\boldsymbol{x}). \tag{1d}$$

The dielectric tensor, $\overleftrightarrow{\sigma}_{\mathrm{c}}$, is an integral function of the particle distribution function, $f_0(\boldsymbol{x},\boldsymbol{v})$, whose time evolution is assumed to be much slower than the RF frequency. This distribution function may be specified as a Maxwellian, in which case the dielectric tensor for a Fourier mode is given in terms of Fried–Conte functions [2, 6] and modified Bessel functions. As discussed in the code references above, the Fourier modes in AORSA allow ion wave physics to be modeled for all orders of of $k_\perp\rho_{\mathrm{i}}$, the ion gyro-radius divided by the perpendicular wavelength. For TORLH, a finite-Larmor radius expansion is employed in the radial dimension. In both codes, the Fried–Conte function is evaluated with a value of $k_\parallel$ formulated in the code basis. With sufficiently strong electric fields, $f_0(\boldsymbol{x},\boldsymbol{v})$ must be evolved in the presence of the RF waves.

The evolution of this distribution function is described by the zero-orbit width, bounce-averaged quasilinear Fokker–Planck (FP) equation that is schematically given by:

$$\frac{\partial f_0(\boldsymbol{x},\boldsymbol{v})}{\partial t}=D+C+L+S, \tag{2}$$

where the right-hand side terms are bounce-averaged wave diffusion (D), collisional diffusion (C), loss (L) and source (S) terms respectively. The solution to this time-dependent problem is performed by CQL3D code [7] that solves for the time evolution of the distribution function in the presence of RF waves for time-scales that are long compared to the particle bounce time [1]. As suggested above, the WE and FE systems may be formally decoupled with wave and bounce periods being much slower than that of the distribution function. Even with this separation, finding self-consistent solutions to the combined WE-Fokker–Planck system has proven to be a challenging task because of the non-linearities in the RF and collisional diffusion operators in the Fokker–Planck model.

When an equilibrium solution for the combined systems is desired, a Picard fixed point iteration scheme between the FP and WE codes, scripted in python, has been used to achieve self-consistency. For the time-dependent problem, an explicit time advance requiring many expensive evaluations of the WE and small time steps has been utilized.

In this paper, we discuss the application of reduced rank extrapolation (RRE) and minimum polynomial expansion (MPE) methods to the equilibrium and time-dependent problems. We show that in the LHRF problem where the steady state is of interest, accuracy and stability can be improved with a few iterations with this method. In case of ICRF waves, an implicit time advance can be achieved also resulting in significant time savings. In both frequency regimes we discuss validation efforts with experiments through the use of synthetic diagnostics. These comparisons indicate the full wave LH simulations capture important effects of interference of the waves present in cases where the absorption of these waves by the plasma is relatively weak. In the simulations of ICRF heating, comparisons of the energy spectrum of heated ions motivate the inclusion of more detailed effects of the ion orbits on the evolution of $f_0(\boldsymbol{x},\boldsymbol{v})$ neglected by the FP code that improve agreement with experiment.

2. Physics of LH and IC waves

2.1. Lower hybrid slow waves for current drive

RF electric fields in the lower hybrid range of frequencies are characterized by $\omega_{\mathrm{LH}}\sim\sqrt{\Omega_{\mathrm{ce}}\Omega_{\mathrm{ci}}}$ where $\Omega_{\mathrm{i,e}}\equiv qB/m_{\mathrm{i,e}}c$ are the ion and electron cyclotron gyration frequencies in a magnetic field of strength B. This frequency is on the order of several GHz at magnetic field strengths of several tesla. These waves have perpendicular wavelengths of the order of 1 mm at densities of the order of $10^{20}\,\mathrm{m}^{-3}$ in a fusion device that typically has scale lengths on the order of 1 m. They are nearly electrostatic with a high phase velocity and interact with electrons at many times the electron thermal speed, given by $v_{\mathrm{te}}=\sqrt{2T_{\mathrm{e}}/m_{\mathrm{e}}}$ where m_{e} and T_{e}

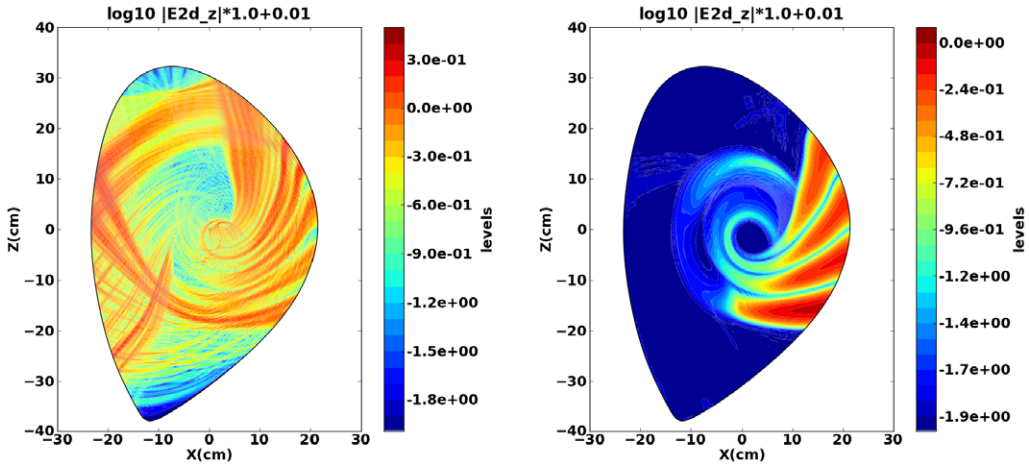

Figure 1. Left panel: TORLH/CQL3D simulation of weak damping regime in Alcator C-Mod ($n_\parallel = -1.6$). Right panel: TORLH/CQL3D simulation of strong damping regime in Alcator C-Mod ($n_\parallel = -3.1$). The magnitude of the two dimensional RF electric field parallel to the magnetic field (|E2d_z|) is shown for a single toroidal mode. The electric field units are arbitrary and are driven by a unit amplitude from four waveguides on the middle right of the plasma cross-section. The plasma parameters ($B_0 = 5.36\,\mathrm{T}$, $n_{e0} = 7 \times 10^{19}\,\mathrm{m}^{-3}$, $T_{e0} = 2.33\,\mathrm{keV}$) were held constant for the two simulations.

are the electron mass and electron distribution temperature, respectively, and v_{te} is the electron thermal speed. Because collisional drag decreases with velocity as $1/v^3$ in plasmas, LH waves are ideal for driving current to control the magnetic configuration. Typically, currents are maintained in fusion plasmas by an external transformer coil with the plasma being the secondary winding, but this is inherently not a steady-state solution.

Because the interaction with electrons takes place at velocities far above their thermal speed, the distribution function is changed from an equilibrium Maxwellian and is instead determined by the balance between collisional and RF wave induced diffusion in velocity space. The evolution of the distribution function in turn affects the dielectric of the plasma and increases the damping of the waves. An iterative scheme, described in detail in section 3.2, is used to achieve self-consistency. In figure 1 we present two cases distinguished by the parallel index of refraction used. Here the parallel refractive index ($n_\parallel$) is defined as $n_\parallel = c/v_\parallel$. Both cases have been iterated to steady state with the CQL3D Fokker–Planck code using fixed point iteration requiring 30 steps for $n_\parallel = -1.6$ and 15 steps for $n_\parallel = -3.1$. The damping is stronger for the higher index of refraction (right panel of figure 1) corresponding to a lower wave phase velocity and thus the distribution function doesn't evolve far from equilibrium. The damping is weaker for the lower index of refraction (left panel of figure 1) and corresponds to an interaction velocity that is significantly relativistic. In this case we can see the unit driving amplitude is increased approximately a factor of 3 ($10^{0.3}$ from the contour scale) in the interior fields because of cavity amplification. Interference structures and reflections are also evident in the weaker damping case of $n_\parallel = -1.6$. These interference structures have an impact on physically measurable quantities such as hard x-ray (HXR) emissions as detailed in section 4.1 and are relevant to current drive experiments having electron temperatures less than approximately 8 keV.

2.2. Ion cyclotron fast waves for minority heating

Ion cyclotron resonance heating (ICRH) of the hydrogen-minority species in a deuterium majority plasma is the prime auxiliary heating scheme on Alcator C-Mod. This heating method is also used on many other tokamaks and a minority hydrogen scheme may be used in the non-activation phase of ITER. Rather than increasing the parallel energy of electrons as in LH, ICRH increases the perpendicular energy of ions at their cyclotron resonance. ICRF also heats electrons in plasmas with significant electron beta through a combination of parallel Landau damping and transit time magnetic pumping, but we will not discuss that further in this paper. The effect of ion heating is shown in figure 2 where the contours of the ion distribution function are strongly distorted along the vertical axis associated with perpendicular energy. The characteristic 'rabbit ear' structure is a consequence of the poloidal variation of the magnetic field that creates a magnetic bottle in that direction with consequentially trapped and lost ions determined by their perpendicular energy and magnetic moment. Heating the minority species with an ICRF wave at the minority ion species fundamental cyclotron frequency is more efficient than heating the majority species at its fundamental frequency because the plasma tends to polarize the ICRF wave opposite of the ion gyration at the location of the majority cyclotron resonance [2]. Energetic ions already present in the plasma or generated by the ICRH itself can influence wave absorption by increasing single pass absorption, modifying the deposition profile and changing the energy partition between electrons and ions. We simulate ICRH interaction with the plasma by coupling the spectral full wave solver AORSA with the zero ion-orbit-width Fokker–Planck code CQL3D. Coupling the codes allows self-consistent solutions that include the effects of energetic ions on the RF fields [8].

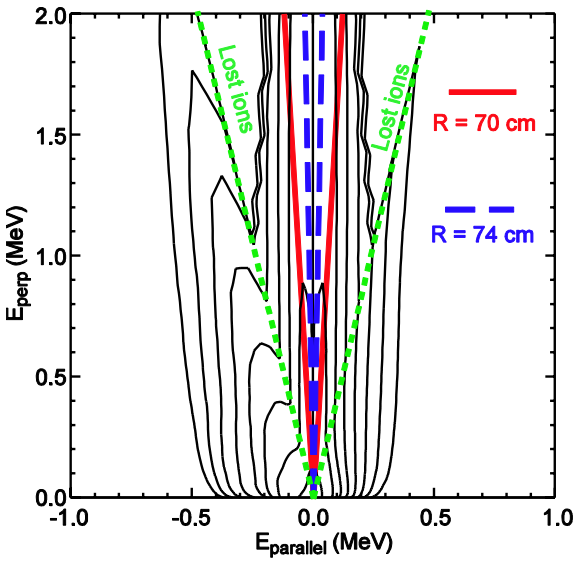

Figure 2. The distribution function resulting from self-consistent coupling between AORSA and CQL3D for a minority heating case shown at a normalized minor radius of $r/a = 0.3$. The green dashed lines indicate the region in momentum space where ions become trapped. The solid red and dash blue lines show which trapped ions are viewed by the compact neutral particle analyzer (CNPA) ion diagnostic discussed in section 4.2.

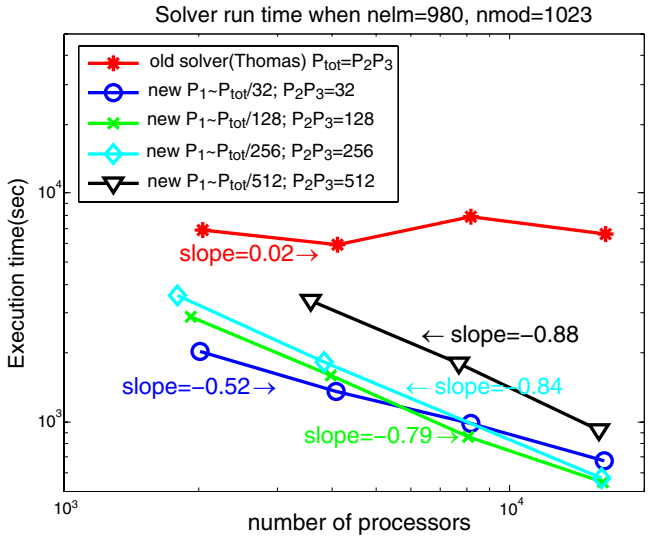

Figure 3. Comparison of execution time of parallel solver for different processor numbers in the two level solver for typical lower hybrid resolution of 980 radial finite elements and 1023 polodial modes. P_1 is the number of processors in the block row direction. $P_2 P_3$ is the number of processors in the two dimensional decomposition of the blocks. The four decompositions shown exhibit some variation in execution time. The three dimensional decomposition is on average 5–10 times faster than the two dimensional decomposition solver and demonstrates much better parallel scaling.

3. Numerical techniques

3.1. Higher order parallelism

We have developed the tools for solving for the self-consistent RF electric fields in the lower hybrid frequency regime [5, 9] as well. The full wave code TORLH, a modified version of the TORIC ICRF code [10], has been made more efficient with a new parallel solver [4, 11] that reduces the execution time a factor of 3–5 for typical runs on 64 to 128 processor cores to the order of 1–2 h. The stiffness matrix that results from the solution of the system in equation (1) using the decomposition in equation (1*b*) results in a block tridiagonal system. Typically this method would suffer from communication saturation as the number of processors was increased. However the two level solver extends the parallelizaton to block rows by replacing the original Thomas solver technique with a partitioned block cyclic method. The methods were implemented using the ScaLAPACK and BLACS parallel linear algebra software stack [12].

As shown in figure 3, this new solver scales to tens of thousands of cores efficiently enabling wall clock times of several minutes. The improvement is due to an avoidance of the strong scaling limit of the direct solve of the blocks by extending the parallelism of the solver along the radial dimension (associated with block rows of the stiffness matrix). This is done using a combination of cyclic reduction and divide and conquer algorithms that are common in tridiagonal solvers [13]. A recent upgrade of the CQL3D code [7] now employs an implicit time advance and is parallel in the radial dimension, bringing run times of this Fokker-Planck code down to the order of a few minutes on 32 cores for problems discussed in this paper. Iteration of these codes produces an electron distribution function and a wave electric field that are consistent with one another.

3.2. Vector acceleration

Equation (3) describes the normal fixed point iteration technique (also known as Picard iteration) used to iterate between two systems. In our case, it consists of a WE which determines the wave electric field as described by equations (1) and FP equation which advances the ion or electron particle distribution (f) in time subject to collisional and wave induced diffusion (D_{ql}) where the later depends on the RF fields solved for by the WE. The values at the $(n+1)$th iteration are given simply from the operators FP and WE at the nth step:

$$f_{n+1} = \mathrm{FP}(f_n, D_{ql_n})$$

$$Dql_{n+1} = \mathrm{WE}(f_n). \qquad (3)$$

This technique is known to converge slowly in many instances. It can also be unstable in cases of weak ($n_\parallel^2 < 40/T_e$) absorption unless used carefully (small time steps in the FP code and ramping up of power slowly.) A vector extrapolation method [14, 15] that permits Jacobian free acceleration of the traditional Picard fixed point iteration technique is used to reduce the number of iterations needed between the distribution and wave codes to converge to self-consistency. This method only requires the solutions resulting from the iterations of the fixed point method and refines the solution to much higher accuracy at negligible cost as shown in figure 4. The solution from fixed point iteration must be sufficiently close to the correct solution to linearize about the exact solution to first

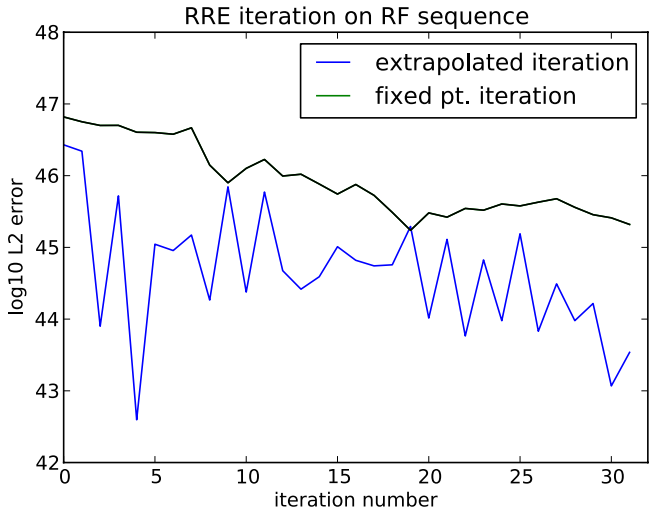

Figure 4. Acceleration of high phase velocity LH iteration implemented in python. The L2 norm of the difference of D_{ql} between successive iteration steps is plotted on a $\log_{10}$ scale. Results have not been normalized to vector norms. Refinement of solution takes less than 10 min with gain in accuracy of more than 50 times ($10^{1.7}$).

order. The Jacobian is the coefficient, $F'(s)$, of the first order term in an expansion of the iteration form of equation (3)

$$x_{n+1} = F(x_n) \approx F(s) + F'(s)(x_n - s), \tag{4}$$

where $x = F(x)$, is the iteration form, s is the true solution and x_n are the results of iteration which in our case are chosen to be the quasilinear diffusion, D_{ql_n}. If the Jacobian was known, we could proceed with a standard Newton's iteration for geometric convergence to the solution. Instead, in vector acceleration, the unknown Jacobian is approximated through a least squares inversion using the iteration vectors generated from the fixed point method. From k iterations, we form the system,

$$\sum_{j=0}^{k} c_j u_j = 0 \tag{5}$$

for the coefficients, c_j, where $u_j = x_{j+1} - x_j$. This system is overdetermined if $j < \texttt{len}(u)$ which is generally the case and may be solved by least squares; here, `len` is the length of the vector. The coefficients, c_j, are the same as the coefficients of the minimum characteristic polynomial of the system matrix, F, and so the technique is referred to as minimum polynomial extrapolation (MPE). Sidi [14] showed these coefficients may be used to approximate the solution as $s = \sum_{j=0}^{k} c_j x_j$. Thus, by determining the coefficients from a least squares problem formed from the original fixed point iterates we may reconstruct a far more accurate approximation from a linear superposition of the iteration vectors. Though not explored here, this technique's performance may be further improved and its memory requirements reduced in practice by applying the extrapolation methods after a fixed number of Picard iterations and then continuing with the iterations.

3.3. Implicit coupling

In the previous section vector acceleration using the RRE technique was used to refine the solution of a fixed point iteration. In this section we apply the MPE version of vector acceleration to extend an explicit time advance of a non-linear system to an implicit one. The FP–WE couplings are non-linear systems with both integral and differential terms. Explicit coupling often requires undesirably small time steps. Using the `AORSA` and `CQL3D` codes in the ICRF regime, we use MPE to resolve the evolution of the ion distribution function in time with an implicit time advance. This is done without modifying or using knowledge of the internal algorithms of the two codes and has been implemented in the integrated plasma simulator (IPS) of the CSWIM SciDAC Project [16].

$$\boldsymbol{E}_{i+1} = \texttt{AORSA}\left(\texttt{CQL3D}_{\Delta t}\left(f_i, \frac{D^i_{\mathrm{QL}}(\boldsymbol{E}_i) + D^{i+1}_{\mathrm{QL}}(\boldsymbol{E}_{i+1})}{2}\right)\right). \tag{6}$$

Conceptually, the implicit solve is a centered Crank–Nicholson advance as given in equation (6). The centering of the quasilinear operator is accomplished by using the MPE algorithm to correct the fixed point iteration between `AORSA` and `CQL3D` to get D^{i+1}_{QL}. Then $D^{i+1/2}_{\mathrm{QL}}$ is used to make the implicit advance of the electric field. The details of this process are enumerated in the following steps:

(i) using distribution function at t_i, use `AORSA` to calculate the RF electric fields, E_i and the associated quasilinear diffusion operator, DQ_i,
(ii) with this diffusion constant, advance f_0 to obtain $f_0(t_{i+1})$,
(iii) find $E^{(j=0)}_{i+1}$ and DQ_{i+1} with `AORSA` (this is the $j = 0$ stationary iteration for E_{i+1}.),
(iv) repeat the advance of $f_0(t_{i+1})$ using $DQ_{i+1/2} = (DQ_i + DQ_{i+1})/2$,
(v) find $E^{(j+1)}_{i+1}$ using $f_0(t^j_{i+1})$ from (iv)—this is the $(j+1)$th stationary iteration for E_{i+1}
(vi) repeat step (iv) step N times generating $E^{(j=1..N)}_{i+1}$,
(vii) use MPE as described in Sidi [14] to develop a new value for E_{i+1},
(viii) test for convergence between MPE generated E_{i+1} and jth iterate: $E^{(j=n)}_{i+1}$,
(ix) if converged, begin a new j cycle at t_{i+1} at step (i), otherwise go to step (iv), using the MPE E_{i+1} instead of the $j = 0$ value and start a new j cycle.

A small number of explicit advances ($j - 1$ steps) are used in conjunction with vector acceleration to produce a time centered RF diffusion (D_{ql}) that is used in an implicit advance. In figure 5, the calculation of the hydrogen distribution energy for the explicit and implicit time advance are compared for different time steps. It is seen that the implicit advance with six time steps, the filled-in points, reproduces the curve using 160 explicit time steps. The MPE implicit advance required 2981 cpu h (2.3 h on 1296 cpus) and the standard fixed point explicit advance used 10368 cpu hours (8 h on 1296 processors) for a speed-up of great than a factor of 3.

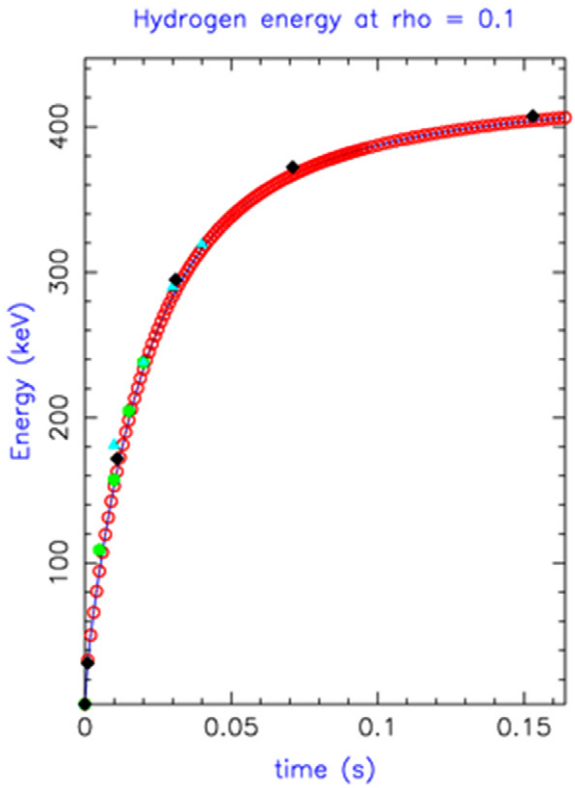

Figure 5. Implicit versus explicit time advance for evolution of minority ion distribution using CQL3D-AORSA codes. The maximum energy on the mesh was 2000 keV. The toroidal mode was $n_\phi = 10$ and the RF power was 2.65 MW. Hollow (red) circles are explicit steps and filled (black) diamonds show using 5 stationary points in each MPE cycle. Filled (green) circles show using four stationary points in each MPE cycle.

4. Synthetic diagnostics and model validation

4.1. HXR emissions for LHRF

On Alcator C-Mod, a HXR camera diagnostic is used to indirectly measure the energy of LHRF accelerated electrons from the bremsstrahlung radiation emitted (via the 'headlight' effect) as they circle the toroidal device—much like in a circular particle accelerator. When the fast electrons pitch angle scatter off of back ground ions and electrons their conical beam of x-rays can be directed along the viewing chords. The diagnostic consists of 32 chords viewing horizontally through a poloidal plane in the plasma and focusing to a detector outside of the plasma [17]. This diagnostic is simulated in the CQL3D code from the calculated electron distribution and is used as a basis of comparison with the experiment. Note that the HXR experimental results shown in this section are for a higher energy range (50 to 90 keV compared to 20 to 40 keV in [18]) and use a revised analysis of the raw HXR data.

The HXR camera [17] measures the bremsstrahlung from high-energy electrons generated through lower hybrid current drive (LHCD). Inherent noise and physical limitations for CdZnTe detectors create a low energy bound for measured photons. Improvements in analysis have shown that low energy photons near the noise floor are more likely to be miss-counted due to their high fractional error in measured energy. These photons are often discarded as noise leading to a sizable variation in count rate, especially in discharges with significant current drive.

Low energy photons in general are more likely to be scattered or absorbed in materials around the tokamak and camera. This increased sensitivity to the local environment can affect the expected distribution of photons, making comparisons between models and experiment more difficult [19] The use of high-Z walls (molybdenum) on Alcator C-Mod also requires avoidance of the possible $K-\alpha$ radiation generated by runaway electron impacts. Extended experimental analysis of HXR data suggests the use of higher energies to better diagnose the electron distribution function for LHCD. Higher energies avoid physical limitations set by the camera, and are much more reliable for computation comparison. Several of these issues are discussed in more detail in [20].

When the absorption strength of LH waves is weak, the waves are in a multi pass regime where interference of crossing waves, reflections from the cutoff and caustic formation must be treated properly. In this case, it is reasonable to expect significant differences between full wave and ray tracing predictions. In figure 6, we compare experimental measurements of HXR emission during LHCD with the HXR predictions for multi pass regime using self-consistent GENRAY/CQL3D and TORLH/CQL3D simulations for the evolution of $f_e(v)$ and calculation of the HXR signal. The HXR signal from ray tracing in the left panel of figure 6 is a factor of five larger than the experiment [18, 21], in contrast to the HXR signal from the full wave analysis. This may be due to the differences in the reconstructed D_{ql} from the two approaches, since the D_{ql} from full wave includes phase interference effects which can lead to a reduction in the energy density that are absent in first order WKB ray tracing. There are also notable differences in the shape of the two simulation profiles and the experimental ones. Both the full wave and the experimental profiles show a hollowness at the central chords consistent with off axis current drive. The ray tracing HXR calculation has flat to peaked profiles resulting from higher on-axis power and current deposition which may be due to the lack of destructive interference in the contribution of the rays to the quasilinear evolution of the electron distribution [22].

In addition, the simulated profiles are both narrower than the experimental ones. The signals in the edge HXR channels (1–5, 25–32) possibly result from scrape-off layer sources [23] that are not included in either the ray tracing or full wave simulation models. Finite Larmor radius effects for electrons are minimal and mostly manifest through possibly enhanced radial diffusion—and even there, that is more a function of field line stochasticity. Studies [18] on the effects of radial diffusion find that is it not sufficient to explain the discrepancy with experiment. Finally it is important to point out that TORLH does not have a scrape-off-layer model extensing out to the vessel wall that accounts for collisional damping of the LH waves which occurs during multiple passes of the wave front in weak damping regimes. The GENRAY ray tracing code [24] and the LHEAF full wave solver [25] do include this effect. However, simulations with GENRAY-CQL3D [24] and LHEAF-VERD [26]

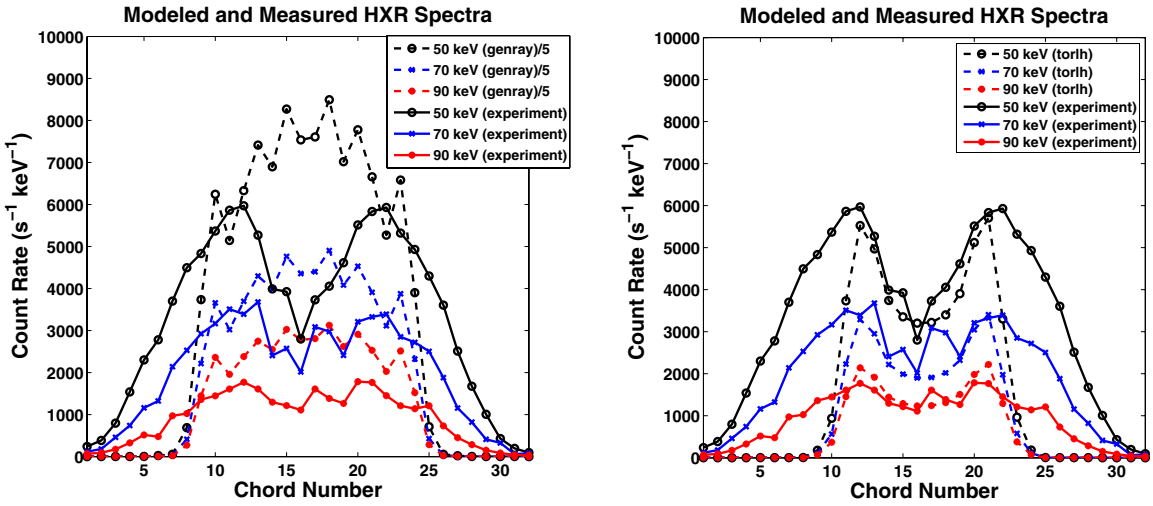

Figure 6. Comparison of measured and modeled HXR profiles for Alcator C-Mod shot 1060728011. Modeled profiles from ray tracing (left panel) have been scaled by a factor of 1/5 and those from full wave (right panel) have not been scaled. The HXR camera views horizontally with chord 1 (32) corresponding to the bottom (top) of the tokamak. Full wave simulations assume 500 kW coupled LH power. The plasma parameters are: $B_0 = 5.36\,\mathrm{T}$, $n_{e0} = 7 \times 10^{19}\,\mathrm{m}^{-3}$, $T_{e0} = 2.33\,\mathrm{keV}$.

in this lower density regime (n_e(line-av) $5 \times 10^{19}\,\mathrm{m}^{-3}$) have shown that edge losses due to collisions are negligible in these discharges.

4.2. Compact neutral particle analyzer for ICRF

The fast-ion distribution created during minority ion cyclotron heating is measured on the Alcator C-Mod device with a compact neutral particle analyzer (CNPA) [27, 28]. The CNPA consists of vertically viewing photodiode detectors with viewing chords from $r/a = 0.18$ to 0.60 and energies from 150 keV to 1.5 MeV. The CNPA measurements are compared to the output of a synthetic diagnostic [27–29] that has been added to the Fokker–Planck solver CQL3D [7]. The synthetic diagnostic calculates the flux of neutrals (in events per second per steradian per cm^2 per keV) along a sightline and provides and indirect measurement of the minority ion distribution during ICRF. Fast ions can neutralize by charge exchange with background neutral deuterium or hydrogen-like boron or by recombination with thermal electrons. Boron is a common impurity in C-Mod and charge exchange with boron is the dominant neutralization process for most of the energy range that is measured in C-Mod [27–29]. The densities of the D^0 and the B^{4+} are specified as inputs to the synthetic diagnostic. These are not measured directly and are instead calculated by the transport analysis code TRANSP (for D^0) and by a collisional equilibrium calculation (for B^{4+}), where the B^{5+} density is assumed to be a constant percentage of the electron density. This percentage is unknown, although spectroscopic measurements estimate it to be ∼1% of the electron density, n_e. In order to produce agreement with the simulation, boron densities of 2.5% are used for all simulations presented in this paper. The synthetic diagnostic is found to be insensitive to variations in electron density, electron temperature or hydrogen fraction, provided that hydrogen fraction is low enough that the waves are not in the strongly mode-converted regime. However, the synthetic diagnostic is very sensitive to sightline placement near the resonance layer. This sensitivity prompts the use of multiple sightlines in order to model a sightline with finite width.

Simulations were performed by iterating AORSA and CQL3D by fixed point iteration until a self-consistent fast-ion distribution is obtained. Time-dependent simulations were advanced in steps of 1ms in the CQL3D code with sub-steps of 0.1 ms. Four simulations of four plasma discharges at currents ranging from 0.6 to 1.2 MA were performed and the results show good agreement between simulation and the CNPA experimental results for all currents. Shown in the left panel of figure 7 are results from a simulations at 1.0 MA. The simulations correctly predict the energy dependence of the fast-ion signal and the relative intensity of signal at the two channels. There is excellent agreement in the steady-state case (left panel) in which the simulation correctly reproduces the energy dependence of the fast-ion signal. Furthermore, there is agreement with the relative strength of the signal on the two channels, showing that it captures the better fast-ion confinement in the high-current plasmas [28].

Though good agreement is obtained between simulation and experiment for fast-ion distributions that are in steady-state ($\mathrm{d}f/\mathrm{d}t = 0$), there are discrepancies between the experimental and simulated results for the time-dependent evolution of the fast-ion distribution. In particular, the experimentally measured rise time of the ion tail is faster than the simulated rise time, which can be seen in the measured spectra shown as dashed lines in the right panel in figure 7. Several reasons for this discrepancy were investigated: finer time-stepping algorithms do not improve the simulation results, the faster rise and decay cannot be explained by changes in boron concentration, and increasing radial diffusion can produce a faster rise and decay, but cannot produce the correct shape with respect to energy regardless of what diffusion parameters are chosen. A possible explanation of the discrepancy is due to violation of certain assumptions of quasilinear theory which assumes successive interactions between the ions and the ICRF

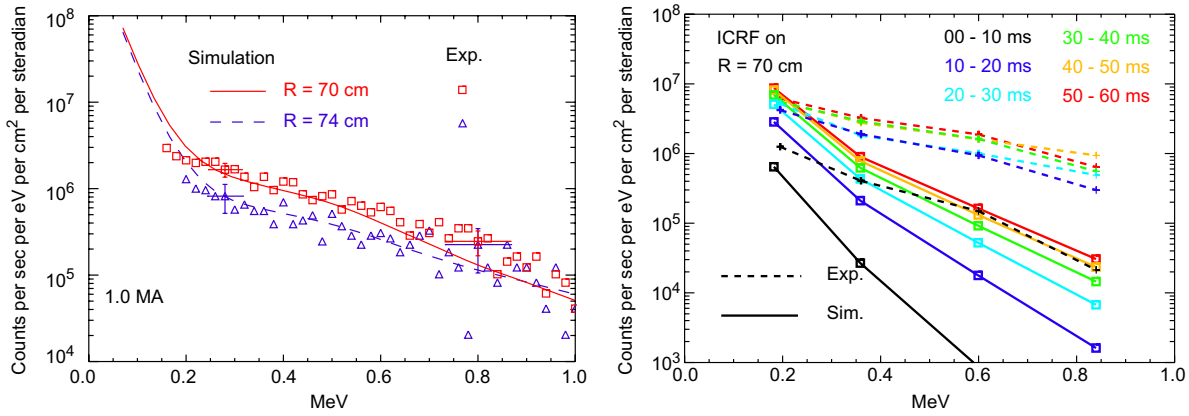

Figure 7. Comparisons of charge exchange neutral flux between simulation and experiments are shown for 1.0 MA plasma current in steady state (on the left) and while evolving (on the right.) The energy distribution of neutrals created by charge exchange with ICRF generated energetic ions is shown in terms of count rate received in a solid angle as a function of energy by the diagnostics. Good agreement in the neutral flux distribution in steady state is shown in left panel while the right panel time slices during an ICRF pulse show discrepancies during the minority ion tail formation.

waves are uncorrelated and that the 'kick' that an ion receives when passing through resonance with the wave produce a small percentage change in its energy [30].

To address the discrepancy in rise time of different energy bins, we use the particle code, DC [31, 32] to calculate the diffusion coefficient directly from single particle motion. Particles are launched equispaced in initial gyro-phase about a given gyro-center and also equispaced in toroidal length. The diffusion coefficients are obtained by averaging the resulting square of the velocity changes after one (or more) particle poloidal circuits, to obtain the ICRF bounce-averaged diffusion tensor. This is carried out for a 3D array $(u_\parallel, u_\perp, R)$ of initial conditions, giving the six independent RF diffusion coefficients in 3D constant-of-motion space. The method follows the formalism of [33, 34]. To isolate the differences with quasilinear theory, the particle orbits were adjusted with fictitious forces that compensated for drifts of particle motion due to magnetic field gradients and curvature. This provides a fair basis of comparison to the zero orbit width model used in calculating D_{ql} from the wave code. The integration of (32 radii) × (128 $u_\perp$) × (256 $u_\parallel$) × (8 gyro-phase) × (32 toroidal angle) starting positions (268M Lorentz orbits) is well-parallelized and takes 7 h on 4096 cores.

Recall that the right panel of figure 7 are results from the time resolved evolution of the ion distribution at three time points during the rise of ion energy as shown in figure 5. The vertical perpendicular viewing chords on Alcator C-Mod are particularly sensitive to the minority ion perpendicular velocity distribution, which is most affected by the enhanced pitch angle scattering calculated with DC due the the retention of correlation effects. In comparing figure 8 and the right panel of figure 7 we see that the DC results bring the energy dependence of the evolution of the distribution function into better agreement with experimental measurements. The application of the DC code to this problem was motivated by the discrepancies between the synthetic diagnostic from the CQL3D code and experiment seen during the minority ion tail formation. Two physics effects neglected in the AORSA/CQL3D coupling are included in the AORSA coupling with DC. Although

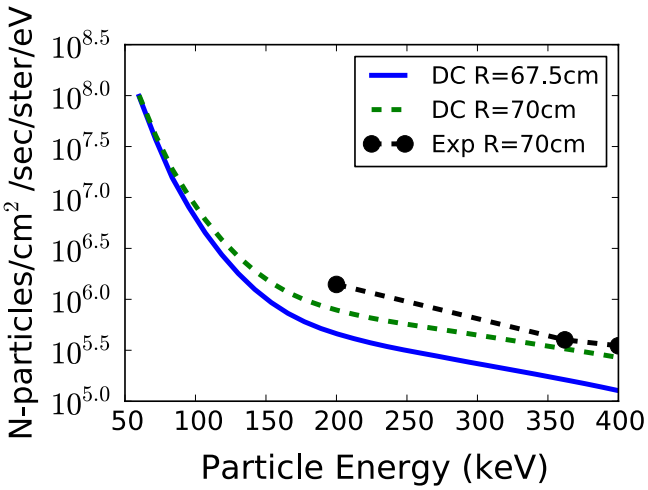

Figure 8. CNPA energy spectra from CQL3D using DC Lorentz orbit based coefficients at $t = 4$ ms. Two vertical view chords at $R = 70$ cm and 67.5 cm at the midplane calculated from CQL3D/DC are compared to the experimental measurement at 0–10 ms for $R = 70$ cm from figure 7. The DC coefficient case for $R = 70$ cm shows excellent agreement with the experimental measurement.

CQL3D uses a zero-FLR approximation, the essential difference in the models lie in DC. The standard coupling with AORSA is done through the Kennel–Engelmann formulation for wave induced diffusion that does not include correlations between successive interactions between ICRF waves and ions or finite orbit effects for the ions. By using a Newtonian push for the ions to evaluate the wave induced diffusion, correlations and finite orbit effects are retained and this accounts for the differences seen in the models. The improved agreement should motivate the development of more efficient algorithms to include the effects without detailed following of orbits.

5. Conclusions

We have presented simulation results from a combined LH full wave/2D $(u_\parallel, u_\perp)$ Fokker–Planck calculation for parameters

characteristic of the weak damping regime in the Alcator C-Mod device. Accurate treatment of the evolution of the distribution function consistent with the wave fields was necessary to achieve these results. We employed vector extrapolation techniques to accelerate the convergence of the self-consistent iteration and showed that the computational burden can be reduced a factor of four to five and the accuracy can be increased a factor of approximately 50. Simulated HXR spectra have been computed from the converged electron distributions predicted by CQL3D and compared against experimentally measured spectra.

AORSA-CQL3D simulations have been performed for Alcator C-Mod minority-heated plasmas and the simulations have been validated by comparing the predictions of a compact neutral particle analyzer synthetic diagnostic with experimental measurements. The results were found to be in good agreement for steady-state plasmas. However, more rigorous time-dependent simulations were found to evolve much slower than the fast-ions in the experiment indicating that quasilinear theory may be violated. Large parallel calculations of the diffusion coefficient directly from the particle orbits results in an evolution of the ion energies that is closer in agreement to the experiment.

For two different frequency ranges of radio frequency waves used in fusion devices, we have done integrated modeling simulations employing advanced mathematical and computational algorithms to introduce new levels of physics fidelity in these models. Through the use of synthetic diagnostics to provide a basis of direct comparison with experiment we have validated these approaches and shown that they result in improved predictive capability.

Acknowledgment

Funding for this research was provided in part under USDOE Contract No DE-FC02-01ER54648.

References

[1] Bonoli P T *et al* 2007 *J. Phys.: Conf. Ser.* **78** 012006
[2] Stix T H 1992 *Waves in Plasmas* (New York: American Institute of Physics)
[3] Jaeger E F, Berry L A, D´Azevedo E, Batchelor D B, Carter M D and White K F 2002 *Phys. Plasmas* **9** 1873–81
[4] Wright J C, Valeo E J, Phillips C K, Bonoli P T and Brambilla M 2008 *20th Int. Conf. on Numerical Simulation of Plasmas, (Austin, TX, 2007) Commun. Comput. Phys.* **4** 545–55
[5] Wright J C, Bonoli P T, Schmidt A E, Phillips C K, Valeo E J, Harvey R W and Brambilla M A 2009 *Phys. Plasmas* **16** 072502
[6] Fried B D and Conte S D 1961 *The Plasma Dispersion Function* (New York: Academic)
[7] Harvey R W and McCoy M G 1993 The CQL3D Fokker–Planck code *Proc. IAEA Tech. Committee Meeting (Montreal, Canada, 1992)* (Vienna: Institute of Physics Publishing) pp 489–526
[8] Jaeger E F *et al* 2006 *Phys. Plasmas* **13** 056101
[9] Valeo E J, Phillips C K, Bonoli P T and Wright J C 2007 Full wave simulations of LH wave propagation in toroidal plasma with non-Maxwellian electron distributions *17th Topical Conf. on Radio Frequency Power in Plasmas (Clearwater, FL)*, vol 933, ed P Ryan and D Rasmussen (New York: American Institute of Physics) p 297
[10] Brambilla M 1999 *Plasma Phys. Control. Fusion* **41** 1–34
[11] Lee J P and Wright J C 2014 *Comput. Phys. Commun.* **185** at press
[12] Blackford L S *et al* 1997 *ScaLAPACK User's Guide* ed J J Dongarra (Philadelphia, PA: Society for Industrial and Applied Mathematics)
[13] Garaud P and Garaud J D 2008 *Mon. Not. R. Astron. Soc.* **391** 1239–58
[14] Sidi A 1991 *J. Comput. Appl. Math.* **36** 305–37
[15] Sidi A 2008 *Comput. Math. Appl.* **56** 1–24
[16] Elwasif W R, Bernholdt D E, Berry L A and Batchelor D B 2007 Component framework for coupled integrated fusion plasma simulation *Joint Workshop on HPC Grid Programming Environments and Components and Component and Framework Technology in High-Performance and Scientific Computing (Montreal)*
[17] Liptac J, Parker R, Tang V, Peysson Y and Decker J 2006 *Rev. Sci. Instrum.* **77** 103504
[18] Schmidt A E, Bonoli P T, Meneghini O, Parker R R, Porkolab M, Shiraiwa S, Wallace G, Wright J C, Harvey R W and Wilson J R 2011 *Phys. Plasmas* **18** 056122
[19] Peysson Y and Imbeaux F 1999 *Rev. Sci. Instrum.* **70** 3987–4007
[20] Meneghini O, Shiraiwa S, Faust I, Parker R, Schmidt A and Wallace G 2011 *Fusion Sci. Technol.* **60** 40–7
[21] Schmidt A E 2011 Measurements and modeling of lower hybrid driven fast electrons on Alcator C-Mod *PhD Thesis* MIT, Cambridge, MA
[22] Wright J C and Bonoli P T 2013 Interference effects on quasilinear diffusion of lower hybrid waves *AIP Conf. Proc.* **1580** 434–7
[23] Baek S G, Shiraiwa S, Parker R R, Bonoli P T, Marmar E S, Wallace G M, Dominguez A, Kramer G J and Lau C 2014 *Phys. Plasmas* **21** 012506
[24] Wallace G M *et al* 2012 *Phys. Plasmas* **19** 062505
[25] Meneghini O, Shiraiwa S and Parker R 2009 *Phys. Plasmas* **16** 090701
[26] Meneghini O 2012 Full wave modeling of lower hybrid waves on Alcator C-Mod *PhD Thesis* MIT, Cambridge, MA
[27] Bader A 2012 Experimental measurements and numerical modeling of fast-ion distributions in the Alcator C-Mod Tokamak *PhD Thesis* MIT, Cambridge, MA
[28] Bader A, Granetz R, Parker R, Bonoli P, Hutchinson I, Sears J and Wukitch S 2012 *Nucl. Fusion* **52** 094019
[29] Bader A, Bonoli P T, Granetz R S, Harvey R W, Jaeger E F, Parker R and Wukitch S J 2011 Fast-ions on Alcator C-Mod: comparisons between simulation and experiment for equilibrium and evolving distributions *AIP Conf. Proc.* **1406** 357–60
[30] Kennel C F and Engelmann F 1966 *Phys. Fluids* **9** 2377
[31] Harvey R W, Petrov Y, Jaeger E F, Berry L A, Batchelor D B, Bonoli P T and Wright J C 2009 Comparison of icrf-induced ion diffusion coefficients calculated with the dc and aorsa codes *AIP Conf. Proc.* **1187** 581–4
[32] Harvey R W, Petrov Y, Jaeger E F and Group R S 2011 Validation studies of quasilinear theory of resonant diffusion in the ion cyclotron range of frequencies by comparison with exact integration results *AIP Conf. Proc.* **1406** 369–72
[33] Kaufman A N 1972 *Phys. Fluids* **15** 1063
[34] Eriksson L G and Helander P 1994 *Phys. Plasmas* **1** 308–14